# Errors in Mean and Fluctuating Velocity Due to PIV Bias and Precision Uncertainties

Brandon Wilson, Barton L. Smith
Utah State University

**Abstract**

Particle Image Velocimetry is a powerful fluid velocity measurement tool that has recently become important for CFD validation experiments. Knowledge of experimental uncertainty is important to CFD validation, but the uncertainty of PIV is very complex and not well understood. Previous work has shown that PIV measurements can become "noisy" in regions of high shear as well as regions of small displacement. This paper aims to demonstrate the impact of these effects on validation data by comparing PIV data to data acquired using hot-wire anemometry, which does not suffer from the same issues. It is confirmed that shear and insufficient particle displacements can result in elevated measurements of turbulence levels.

## 1 Introduction

Nuclear safety increasingly relies on numerical modeling and simulation (M&S), particularly computational fluid dynamics (CFD), as a tool to improve reactor design and safety. CFD and M&S have been used for applications such as accident scenario predictions, plant efficiency, and others. One obstacle to implementing M&S for the advancement of nuclear technology is validation. The CFD Best Practice Guidelines [1] from the NEA states that validation of nuclear M&S must be attained by comparison to experimental data; alternative guidelines are suggested by Lee and Bauer [2] in which CFD should be validated with validation-level experiments and datasets. These guidelines state that validation-level datasets should be acquired using non-intrusive measurement techniques and provide a complete uncertainty analysis of the validation metrics.

Particle Image Velocimetry (PIV) is a powerful, full-field, non-intrusive velocity measurement technique for single phase and some two-phase flows. While other non-intrusive techniques exist (such as Laser Doppler Anemometry), no other provides the full velocity field at an instant in time.

A common, but incorrect, practice for quantifying PIV uncertainty is to estimate a maximum uncertainty for the flow field and apply it globally to the entire field. This will inevitably overestimate the uncertainty in most of the flow field, rendering the data unsuitable for CFD validation. Two efforts have been made recently to calculate these uncertainties locally. Timmins et.al. [3, 4] have studied the effects of particle density, size, displacement, and flow shear and rotation and the correlation between these sources to determine the PIV uncertainty for each vector (in space and time) in a measurement set. They reported that these four parameters could each generate bias and fluctuations in the measurement, similar to the results of Raffel *et al.* [5]. A broader approach with less emphasis on uncertainty from the PIV algorithm was recently presented by Lazar *et al.* [6] but found uncertainty values that were much smaller.

Most flows of interest contain regions with variable levels of uncertainty throughout the measurement field. M&S validation requires accurate assessments of the localized uncertainty. For example, consider a jet exit. This flow contains regions of high shear at the edges of the jet, which generate large amounts of "noise" in the PIV measurement [4, 5], while smaller uncertainties are located within the core region of the jet where low shear and nearly uniform profiles are observed. While the effect of this noise on the time-averaged velocity can be eliminated by increasing the number of samples acquired, its impact on turbulent statistics, which are also important to CFD validation, cannot. Under this and similar situations, a global uncertainty would give an unrealistic measure of the full measurement field.

## 1.1 Velocity Fluctuations

The application of PIV to M&S validation requires accurate measurement of velocity statistics, such as velocity means and fluctuations. While uncertainties on the mean due to velocity fluctuations and PIV noise may be reduced by acquiring increased quantities of data, measurements of the fluctuation levels will always increase with measurement error. This phenomena will be discussed later, but this fluctuation error must be quantified prior to using PIV data for validation purposes. In many situations, PIV data is used to provide inlet conditions to CFD models or global and local quantities. The data acquired ranges from mean velocities to turbulence statistics. Turbulence statistics are measured by the fluctuations within the measurement and, as such, are susceptible to elevated fluctuation levels due to measurement error. It is impossible to validate a CFD simulation that is expected to predict these elevated fluctuation or turbulence levels.

Measured velocity statistics (mean and rms) are affected differently by errors on the measured data. It may be assumed that a measured variable is composed of three components, the mean ($\overline{u}$), the actual velocity flucutations ($u'$) such as turbulent fluctuations, and random, non-physical noise or measurement uncertainty ($\breve{u}$). The measured or total fluctuations may then be written as $\hat{u} = u' + \breve{u}$. Using this relation, the measured velocity ($u$) at any spatial and temporal location is obtained through the sum of the mean and measured fluctuations components,

$$u = \overline{u} + \hat{u} = \overline{u} + u' + \breve{u}. \tag{1}$$

Considering $\breve{u}$ should be somewhat centered around $\overline{u}$, the effect of random measurement uncertainties on the mean is minimized as the number of data acquired is increased. However, this is not the case for fluctuations or rms measurements, in which an increased measured fluctuation is always observed for non-zero measurement uncertainties. For simplicity, it is assumed the mean value of $u$ is zero; the mean total fluctuations are now,

$$\overline{\hat{u}\hat{u}} = \frac{1}{T}\int_0^T \left(u' + \breve{u}\right)^2 dt = \frac{1}{T}\int_0^T \left(u'^2 + \breve{u}^2 + 2u'\breve{u}\right) dt. \tag{2}$$

When these components are time averaged, assuming the measurement uncertainties and velocity flucutations are not correlated, the cross terms disappear and the mean total fluctuations become,

$$\overline{\hat{u}\hat{u}} = \overline{u'u'} + \overline{\breve{u}\breve{u}}. \tag{3}$$

Noting that $\breve{u}$ is a measure of the size of the measurement uncertainty, any component generating these measurement uncertainties will always contribute to the total fluctuations. Often, the measured fluctuations or rms of a flow are reported as turbulence statistics without regard to the error generated from measurement fluctuations. Cases in which this may apply are experimental studies for numerical (CFD) validation. When the effect of measurement uncertainty fluctuations are not considered, an elevated level of turbulence is reported. Due to the number of components that generate uncertainty in PIV, quantifying this fluctuation error is of significant importance to the application of PIV.

The experimental cases studied are designed to not only demonstrate components contributing to PIV errors, but to also demonstrate and quantify the measurement uncertainty fluctuations and their effect on increased rms and measured levels of turbulence.

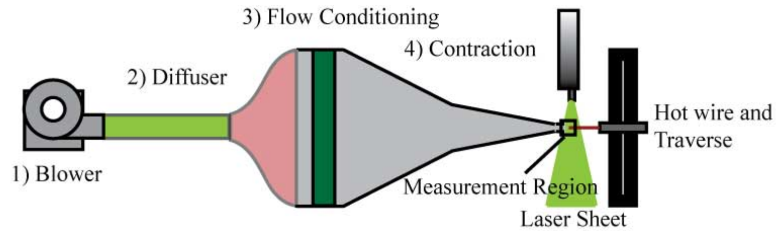


Figure 1: The experimental consists of four components: 1) blower, 2) diffuser, 3) flow conditioning, and the 4) contraction. Hot wire and PIV measurements were acquired downstream of the jet exit. A stepping motor traverse relocated the hot wire measurements along the jet profile. PIV measurements were obtained in the region designated as interrogation region. The PIV camera was located directly in front of interrogation region.

## 2 Experimental Setup

The facility used for this study was originally designed for a different and unusual purpose, and therefore has some unorthodox features. It was chosen because it is capable of producing a high-Reynolds number laminar flow with regions of high shear. The experimental model consists of four components (see Fig. 1): 1) blower, 2) diffuser, 3) flow control, and the 4) contraction. Air exits the channel into the lab environment. Both the jet and lab environment are at same atmospherical conditions. The mean atmospherical air properties at the Experimental Fluid Dynamics Lab (EFDL) based on local barometric pressure, humidity, and temperature are $\rho = 1.0048 \pm 0.00325$kg/m$^3$ and $\mu = 1.89 \times 10^{-5} \pm 1.94 \times 10^{-8}$kg/m-s. Atmospheric quantities are monitored during acquisition of data to ensure similar conditions for both hot wire and PIV measurements.

The blower draws air from the lab environment and into the diffuser section of the experimental model. At this point flow enters a flow control region made from foam to dampen any oscillations and smooth the flow. A two-piece contraction follows, the downstream end of which forms the jet exit. The height at the exit is $H = 9.525$ mm and has a depth of $8H$. The unique contraction is designed to provide a nearly uniform laminar profile at the jet exit for Reynolds numbers of up to Re$= 60,000$ with approximately 70% of the jet profile within 0.5% of the maximum velocity. To expose the measurement fluctuations, $\breve{u}\breve{u}$, it is necessary to minimize the actual fluctuations, $u'u'$, within the jet. Laminar flow within the jet core is indicated by turbulent fluctuations $\left((\hat{u}\hat{u})^{1/2}/u_{max}\right)$ within the jet core below 3%. The jet profile at the exit (shown in Fig. 2 and measured using a hot wire) exhibits laminar flow with regions of high shear at the jet edges and uniform flow in the jet core. One side of the jet exit terminates upstream of the other, leading to non-symmetric fluctuation profiles at the jet edges. This asymmetry has no impact on the present study.

Velocity profiles at the jet exit were measured using a single wire hot wire and particle image velocimetry. Both hot wire and PIV measurements were made in the same plane at the center of the jet. Hot wire measurements were acquired using Labview 10, a single wire probe, and a TSI IFA 100 Hot Wire Anemometer. A response of 10$\mu$s was observed in the hot wire signal. The hot wire was attached to a stepper-motor-operated traverse (accurate within $\pm 5\mu$m) and was used to position the hot wire at discrete locations along the jet profile. At each location, $N = 262144$ measurements were obtained and a sampling rate of $f = 10,000$ Hz. Jet profile measurements were acquired at two locations downstream of the exit: $x = 0.1H$ and $1.25H$. In this manner, two accurate and resolved profiles of the flow were measured with different magnitudes of shear.

PIV measurements were acquired in the same plane as the hot wire measurements using a 12-bit, $1376 \times 1040$ pixel Imager Intense CCD camera and a New Wave dual-cavity 50 mJ /pulse Nd:YAG laser. This system was controlled with DaVis 7.2 from LaVision [7] and seeded using oil droplets uniformly

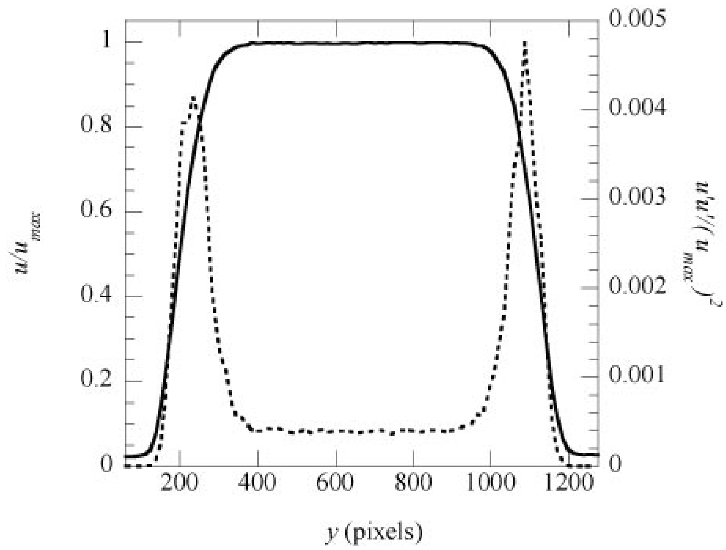


Figure 2: The velocity and turbulence profiles of the laminar jet. The jet exhibits regions of high shear at the jet edges and uniform laminar flow at the jet core. Non-uniformities between jet edges have negligible effect on the PIV uncertainties within this study.

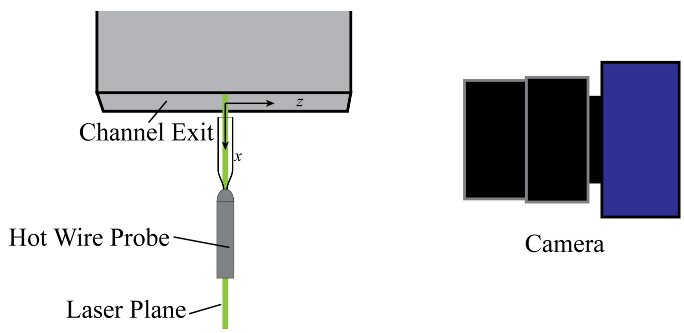


Figure 3: The locations of the instrumentation in the experimental setup. The laser sheet and hot wire probe are located in the same plane with the camera positioned normal to the laser sheet.

distributed at the blower inlet. To obtain converged fluctuation statistics, $N = 1000$ images were acquired at an average of $f = 3$ Hz. The spatial resolution for these images were $0.0108\mu$m/pixel.

PIV images were processed using two PIV algrothms: DaVis 7.2 from LaVision [8] and PRANA from Virginia Tech [9, 10]. Images processed using the DaVis algorithm were processed with square interrogations regions with an initial window size of 32×32 and with two consecutive passes at 16×16 using a 2D SCC algorithm. All interrogation regions were overlapped by 50%. Results were then post-processed using four parameters [7]: an allowable pixel range (vectors displacing more than 15 pixels are rejected), correlation peak ratio, neighboring vectors median filter, and small groups (spurious vectors in groups smaller than 5 vectors are thrown out). Image processing from the PRANA algorithm used the same settings used in [4] for the robust phase correlation (RPC) method [9, 10].

Given the accuracy of the slider stages, images of the hot wire at multiple known locations were acquired and used to calibrate the PIV images. Profiles from the PIV data were extracted at the hot wire downstream locations for direct comparison to the hot-wire results. The hot-wire images provided an accurate method of determining the PIV profile locations.

A single wire hot wire is sensitive to both the streamwise ($u_x$) and spanwise ($u_y$) velocity components, and therefore its output is essentially the magnitude of the velocity in the $x$ and $y$ directions.

However, PIV data measures both velocity components individually and a method of comparing velocity magnitudes and fluctuations is needed. While this is simple for the velocity magnitude ($u^2 = {u_x}^2 + {u_y}^2$), the relation to combine the fluctuations is not as straight forward. The relationship between the two component fluctuations and the fluctuation magnitude is shown in Appendix Appendix A to be:

$$u'u' = \left[u'_x u'_x + u'_y u'_y\right], \tag{4}$$

where $u'_x u'_x$ and $u'_y u'_y$ are the velocity fluctuations in the $x$ and $y$ directions and the fluctuations in the velocity magnitude are denoted by $u'u'$.

All hot-wire velocities are also converted to pixels (using the PIV calibration constant) to allow for direct comparisons. Hot wire measurements were accurate to within ±5%. PIV results are given in dimensions of pixels for pixel displacement (velocity) and spatial coordinates and pixels/pixel for gradients to remain consistent with [4].

# 3 Results

Timmins *et al.* [4] discuss several factors causing PIV uncertainty, including particle image size, particle displacement, particle density, and shear. Local uncertainty due to these sources were determined using synthetic PIV images. The purpose of this paper is to examine these same components using actual experimental data to demonstrate their effects on PIV uncertainty. The particle displacement is varied by changing the time increment between the PIV images (Δt). The seed density ($d_\rho$), particle image size ($d_\tau$), and shear are also varied.

Each of the uncertainty sources mentioned above generate a magnitude of total measured fluctuations ($\hat{u}\hat{u}$) above the "true", turbulent fluctuations ($u'u'$). This will be especially apparent when the true fluctuations are small (due to the apparent fluctuations being the root sum of the actual fluctuations and the PIV noise). For the particle displacement and gradient cases, the "true" fluctuations are measured from the hot wire measurements. By rewriting Eqn. 3:

$$u'u' \approx \hat{u}\hat{u} - \breve{u}\breve{u}, \tag{5}$$

it can be seen that, assuming that the turbulent and measurement fluctuations are not correlated, the measured fluctuations will always overpredict the true fluctuations. With this in mind, the uncertainties on the total fluctuations presented later will be one-sided and negative.

Uncertainties on the total fluctuations are calculated from measurement fluctuations estimated by Timmins *et al.* [3, 4] for the PRANA algorithm (to which they are specific) and Raffel *et al.* [5] for the DaVis algorithm. No uncertainty information on the four PIV uncertainty contributors studied here exists for the DaVis algorithm . The uncertainties within Raffel *et al.* [5] are general and may not be adequate for a complete uncertainty analysis on a particular PIV algorithm; however, an estimate of the uncertainty from each component may be assessed.

The effects of each uncertainty component are discussed next. The data acquired is designed to emphasize individual uncertainty sources; however, due to the nature of the jet (Fig. 2), gradient effects are observed at the jet edges for all cases. For regions with multiple uncertainty sources (*i.e.* jet edge), the uncertainties are combined using the root-sum of the individual uncertainties. In these regions, only the left side of the profile (the lower side of the jet in Fig. 1) will be shown to improve clarity. At the core of the jet, the random uncertainty is dominated by individual uncertainty sources, which can be controlled and varied systematically. To demonstrate the effect of individual uncertainty sources on the measured fluctuations, the measured fluctuations along the centerline of the jet are plotted as a function of the uncertainty source for each case.

### 3.1 Effects of Particle Displacement

The time interval between consecutive images ($\Delta$t) determines the particle displacement for an image set. As PIV displacements become small, the noise associated with subpixel displacements [11] becomes significant. This can be seen in the PIV results obtained for seven cases of varying particle displacement corresponding to maximum displacements of approximately 1, 1.8, 3.7, 5.5, 7.4, 8.4, 9.2, and 10.5 pixels (Fig. 4). Vectors are obtained using the two PIV algorithms (DaVis and PRANA) and a $16 \times 16$ pixel final interrogation region.

The time-mean velocity magnitude agrees for all cases and also match the hot-wire result well (within 2%). However, significant error can be seen in the fluctuation levels except when the displacements are very large. To improve clarity, uncertainty levels are only shown for $dx \approx 1.8, 3.7$, and 5.5 pixels. Although these results are not shown, exceeding 10-pixel displacement resulted in loss of correlation (due to out of plane turbulent motions) and many bad vectors leading to conditional averaging and very elevated fluctuation levels. We conclude that large error in the fluctuation level is introduced using pixel displacements smaller than $\frac{1}{4}$ and larger than $\frac{5}{8}$ the interrogation region size. For the small displacements, the noise associated with sub-pixel estimation is become important.

These errors are the fluctuation levels are caused by "noise" in the PIV measurement and therefore have less impact on the time-averaged velocity. Some bias is evident at low particle displacements. Several important features are observed. First, it is clear that the rate of shear at the edges of the jet is large enough that some "smearing" occurs due to the size of the PIV interrogation regions (we note that the hot wire sensor is very small in the $y$ direction compared to the PIV interrogation region). The time-averaged velocity is well converged for displacements greater than 5 pixels, but becomes less converged and biased for shorter displacements.

Hot wire fluctuations ($u'u'$) are within the uncertainty bars accounting for particle displacement. The size of the uncertainty bars also decrease for larger particle displacements, since the subpixel displacement becomes a smaller part of the measurement (in other words, the dynamic range of the measurement is improving).

Along the centerline, the dominant uncertainty source is due to particle displacement. In Fig. 5 measured fluctuations are shown as a function of increased particle displacement for both the PRANA and DaVis algorithms and compared to the hot wire results. For both Fig. 4 and Fig. 5 hot wire results are within the uncertainty bars accounting for particle displacement. The size of the uncertainty bars also decrease for larger particle displacements.

### 3.2 Effects of Particle Density

Particle density is defined by the number of visible particles within each interrogation region. The effects of particle density on PIV measurements is studied using particle densities of $d_\rho \approx 2.5, 3.5, 4, 5,$ and 7 particles/final interrogation region. This density was estimated from the average number of particles over 16 interrogation regions of size $16 \times 16$ at the center of the jet at $\frac{1}{8}$ the maximum intensity of the camera. At the most dense case ($d_\rho \approx 7$ particles/interrogation region), particle images began to blend and to be composed of multiple particles.

As is clear in Fig. 6 and Fig. 7, particle density has very little impact on either the bias error or the fluctuation levels. Only for the smallest particle density of approximately 2.5 particles can any change in the fluctuation level be detected. As would be expected, particle densities smaller than this would cause even larger errors.

### 3.3 Effects of Particle Image Size

Another contributor to the random uncertainty of a PIV measurement is particle image size, $d_\tau$, which easily controlled by optical settings such as the f-number, $f^{\#}$. Eight data sets with varying particle

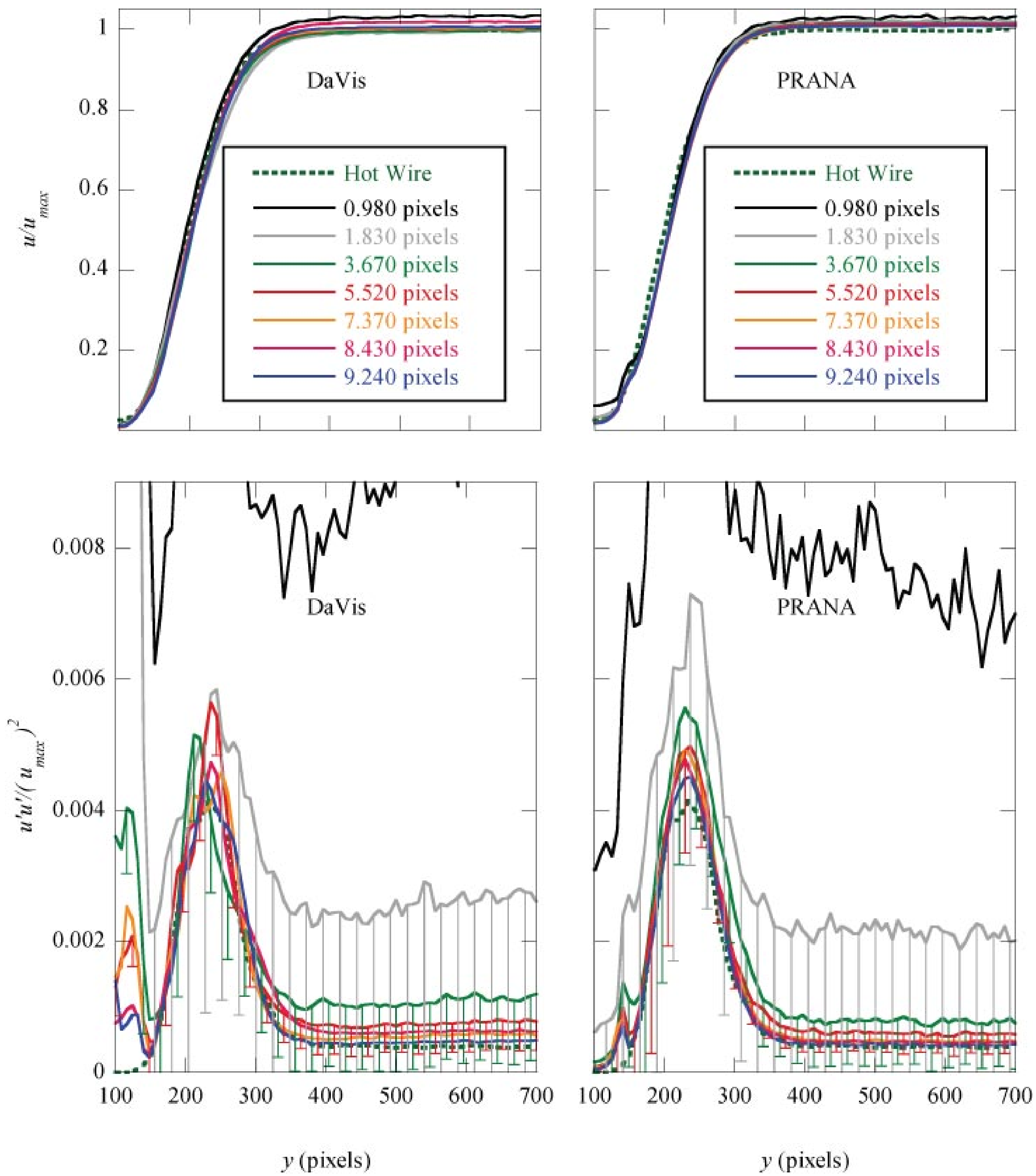


Figure 4: Profile of the velocity magnitude, $u$ (top), and the magnitude fluctuations fluctuations, $\hat{u}\hat{u}$ (bottom), using the DaVis (left) and PRANA (right) algorithms with $16 \times 16$ pixel interrogation regions for varying pixel displacements: $dx \approx 1, 1.8, 3.7, 5.5, 7.4, 8.4$, and 9.2 pixels.

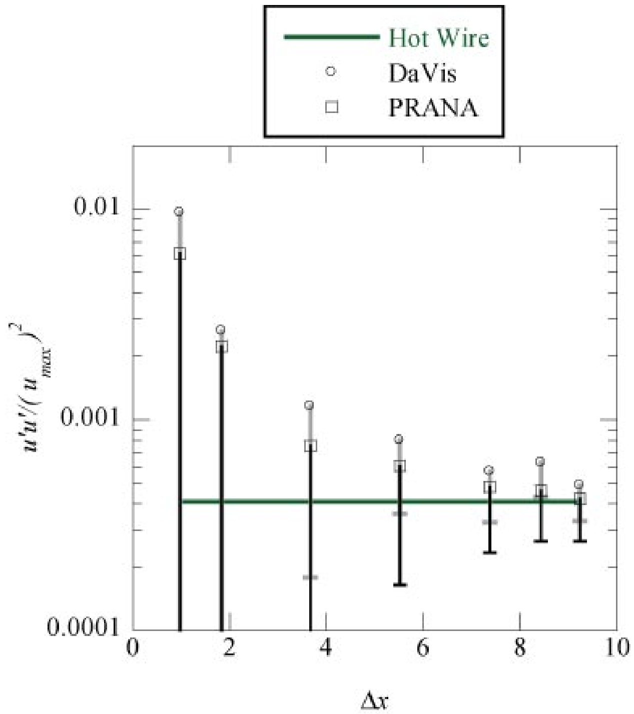


Figure 5: Magnitude fluctuations $\hat{u}\hat{u}$ from the hot wire and PIV algorithm (DaVis and PRANA) measurements for varying particle displacements, $\Delta x$. Fluctuation levels are overpredicted for small particle displacements, however, these are within the uncertainty limits.

image size ($d_\tau = 0.6, 0.9, 1.3, 1.8, 2.5, 3.7, 5.1,$ and $7.5$ pixels) were obtained to demonstrate the influence of particle image size on PIV random uncertainty (shown in Fig. 8). The particle image size is influenced by the$f^{\#}$ through the equation [12],

$$d_\tau = \sqrt{M^2 d_p^2 + d_s^2}, \tag{6}$$

where $M$ denotes the magnification of the image, $d_p$ is the actual particle diameter, and $d_s$ is the diffraction-limited spot diameter defined through,

$$d_s = 2.44\,(1 + M)\, f^{\#} \lambda. \tag{7}$$

In the previous equation, $\lambda$ is the wavelength of the light sheet and $f^{\#}$ is the ratio of the lens focal length, $f$, and aperture diameter, $D_a$.

Particle image sizes were modified by varying the $f^{\#}$ of the camera lense while maintaining equal seed density and image intensity. Seed densities and image intensities were controlled through modifications in laser power and seed quantities. A control image at the smallest $f^{\#}$ ($f^{\#} = 2.8$) was acquired and densities and intensities were visually matched for subsequent image sets. Verification of seed density and image intensity was achieved by monitoring the mean and standard deviation intensities over the entire image.

While particle image size has little effect on the time-averaged velocity magnitude, $u$, the measured fluctuations increase at small ($< 2$ pixels) and large ($> 4$ pixels) particle image sizes (Fig. 9). At all cross-stream positions, the magnitude of the measured fluctuations converge to minimum fluctuation levels measured by the optimal particle size cases of $d_t = 2.5$, and 3.7 pixels cases. Fig. 8 demonstrates, in the region of increased shear, the $d_\tau = 2.5$ pixels case shows decreased fluctuations compared to all other cases, while at the jet centerline, both the $d_t = 2.5$, and 3.7 pixels cases perform similarly. The

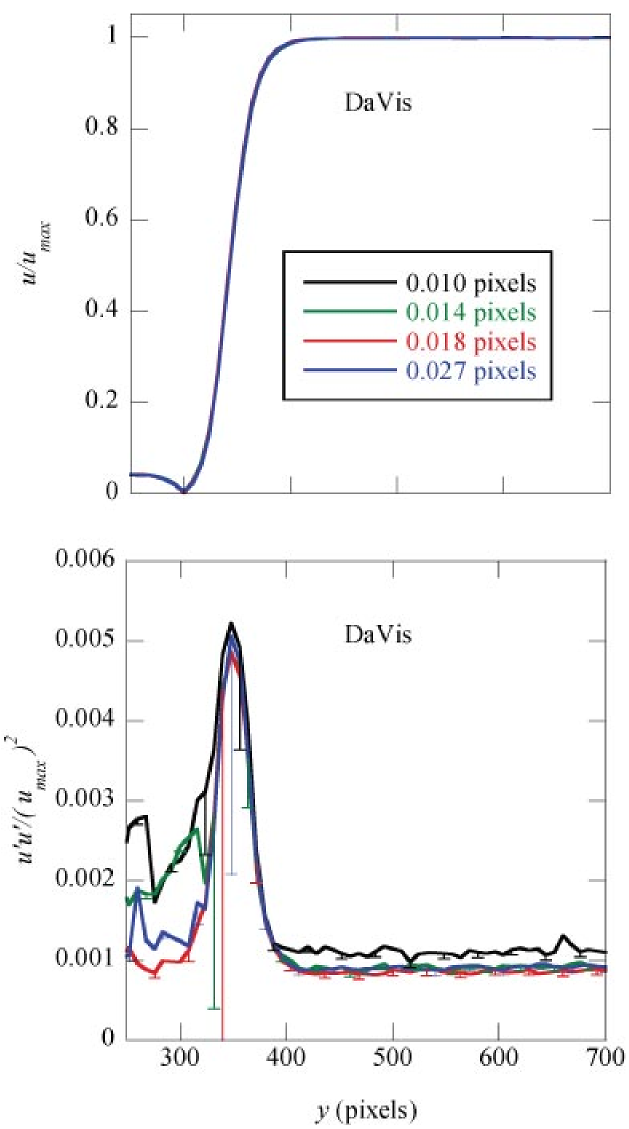


Figure 6: Cross stream profiles of the time-averaged velocity magnitude, $u$ (top), and magnitude fluctuations, $\hat{u}\hat{u}$ (bottom), for various seeding levels stated in average particles per interrogation region.

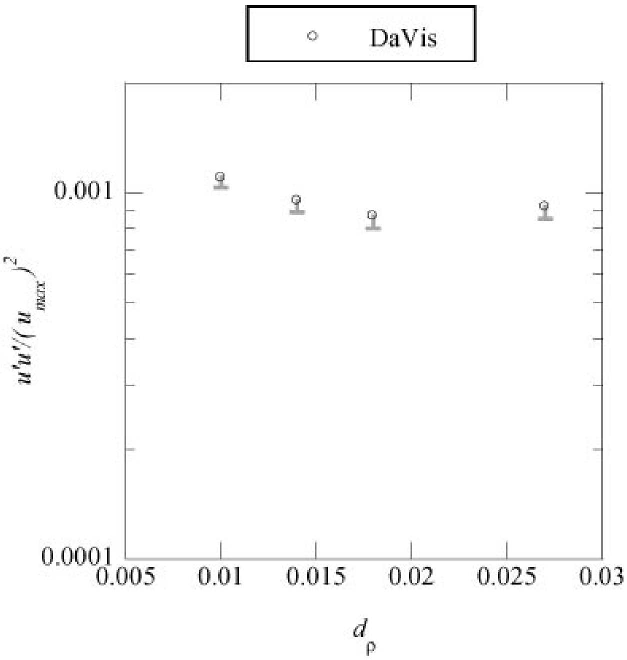


Figure 7: Magnitude fluctuations $\hat{u}\hat{u}$ from the hot wire and DaVis algorithm measurements for varying seeding densities, $d_\rho$. Fluctuation levels are overpredicted for low seeding densities, however, the fluctuation levels are only slightly influenced by seeding density.

overlap of uncertainty bars at the center of the jet demonstrate particle size uncertainties account for the majority of measurement fluctuations within the PIV measurements.

The influence of particle image size on measured fluctuations at the centerline is better observed in Fig. 9 with the fluctuations shown as a function of particle size. The trend shown in Fig. 9 agrees with previous studies (*e.g.* [3, 4, 5]), however, the optimal particle size in this study is slightly larger.

## 3.4 Effects of Shear

Of the error contributers studied by Timmins *et al.* [4], the largest uncertainties were found to be due to velocity gradients (or shear) in the flow. Although shear will affect uncertainty of other algorithms, the magnitude will likely differ. Algorithms including window deformation can reduce the error due to shear.

Data were acquired for two different cases in which the shear levels at the jet edges were observed to be approximately 0.09 and 0.14 pixels/pixel and zero in the jet core. From Timmins *et al.* [4], these shear levels should generate uncertainties of 0.2 and 0.5 pixels at the regions of maximum shear for the PRANA algorithm. Hot-wire, DaVis, and PRANA profiles of the mean velocity $u$ are shown in Fig. 10 for the shear level cases of 0.09 and 0.14 pixels/pixel. A similar trend to the pixel displacement and seed density cases is observed in the data. For all cases, accurate measurements of the mean velocity magnitude are obtained. Velocities at the jet centerline compare well between hot wire and PIV measurements. In the high shear region, the PIV profiles tend to be smeared or smoothed due to PIV averaging over the interrogation region. This effect, however, is small and has little impact on the mean profiles.

Profiles of the fluctuations, $\overline{u'u'}$ for both shear cases are also shown in Figs. 10. These profiles consist of a core region with no shear and small velocity fluctuations and the jet edge regions that contain varying levels of shear. In these regions of high shear, elevated levels of measured fluctuations are expected from gradient errors. As the gradient increases, the DaVis and PRANA algorithms begin

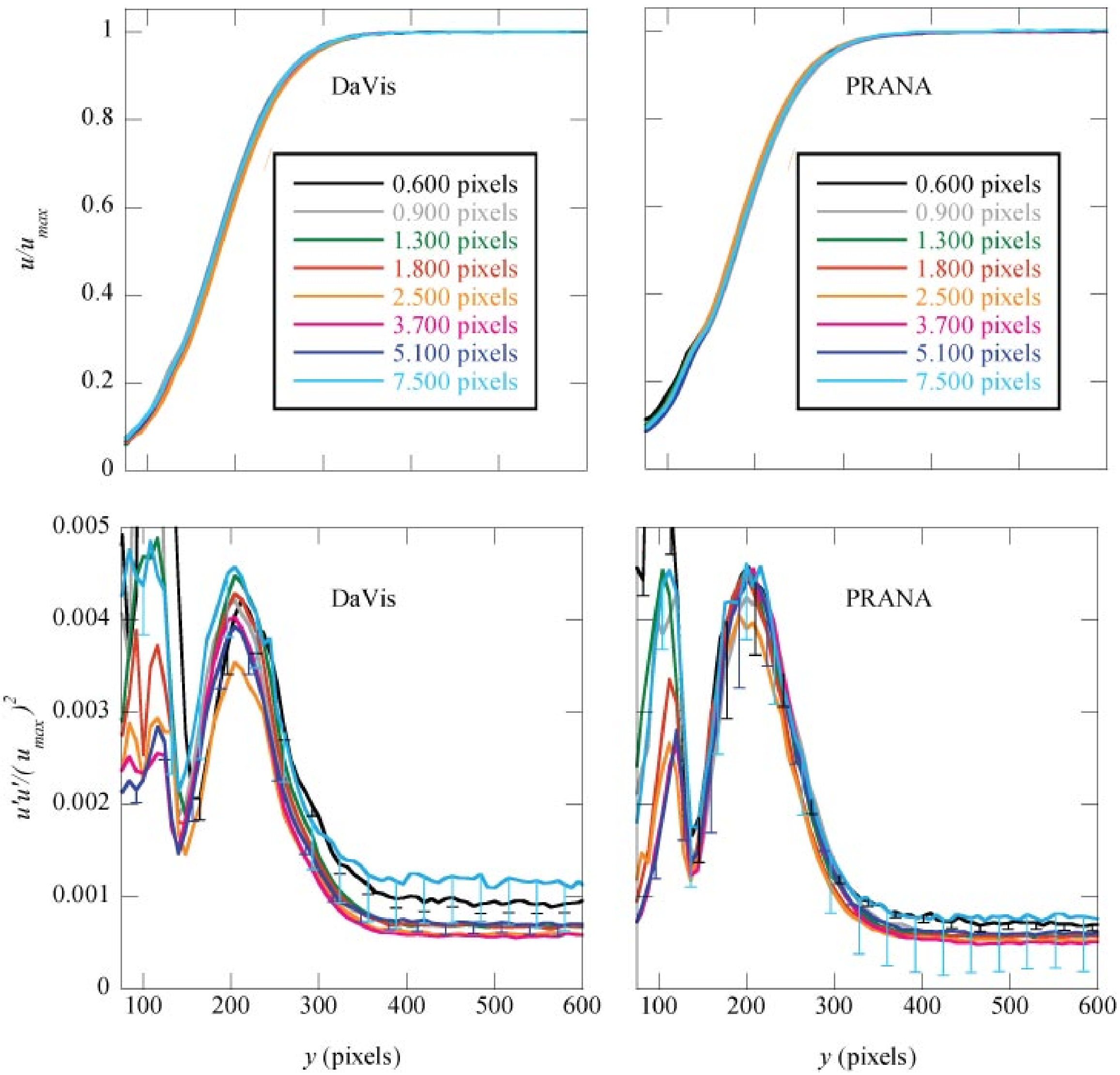


Figure 8: Profile of the velocity magnitude, $u$ (top), and the magnitude fluctuations fluctuations, $\hat{u}\hat{u}$ (bottom), using the DaVis (left) and PRANA (right) algorithms with $16 \times 16$ pixel interrogation regions for varying particle image sizes: $d_\tau = 0.6, 0.9, 1.3, 1.8, 2.5, 3.7, 5.1$, and 7.5 pixels.

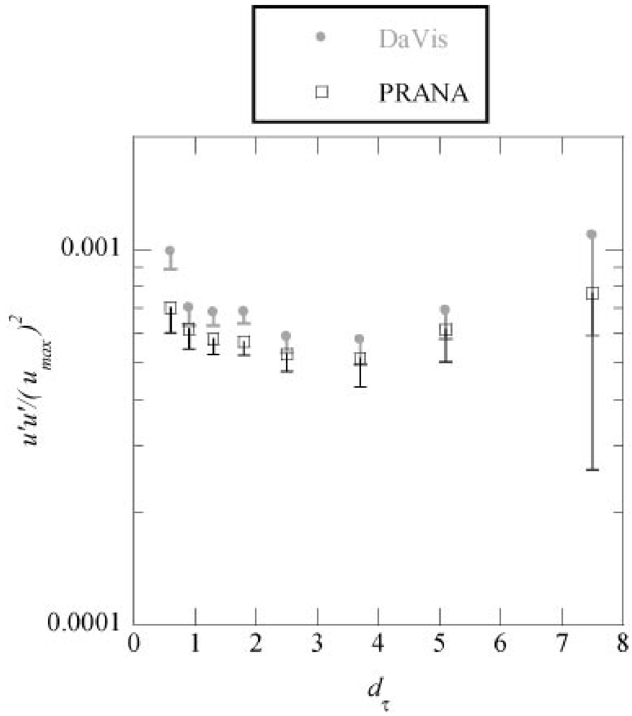


Figure 9: Magnitude fluctuations $\hat{u}\hat{u}$ from the hot wire and PIV algorithm (DaVis and PRANA) measurements for varying particle image sizes, $d_\tau$. Fluctuation levels are overpredicted for small and large particle sizes. The optimal particle image size is found to be between $d_\tau = 2.5$, and 3.7 pixels.

to deviate from the hot wire results and experience elevated fluctuation levels. Uncertainty bars on the total fluctuations caused by the flow gradients show the measurement uncertainty fluctuations ($\breve{u}\breve{u}$) contained within the PIV results are composed primarily of uncertianties from gradients within the flow.

For the $du/dy \approx 0.14$ pixels/pixel case, the difference in total ($\hat{u}\hat{u}$) and measurement uncertainty ($\breve{u}\breve{u}$) fluctuation level agrees well with the hot wire results or turbulent fluctuations ($u'u'$) for both algorithms. Once again, the uncertainty fluctuations, $\breve{u}\breve{u}$, are only applicable for the PRANA algorithm. Although an elevated level of mean total fluctuations is observed in the DaVis algorithm, the increase in magnitude is approximately a factor of two smaller than the PRANA algorithm. The agreement of the corrected fluctuation level from the PRANA algorithm and the hot wire results lead us to believe the dominant component contributing to the elevated fluctuation levels is the shear. This is not the case for the $du/dy \approx 0.09$ pixels/pixel case, in which the corrected velocity fluctuations are larger than that observed by the hot wire results. These results were acquired in a region that vortical structure began to form. For both cases, the estimate of measurement uncertainty from Raffel *et al.* [5] is not as accurate as the estimates for PRANA. This is due to those uncertainties being calculated from a seperate PIV algorithm than DaVis. Timmins *et.al.* [3, 4], however, calculated uncertainties for only the PRANA algorithm.

## 4 Conclusion

PIV errors originated by the PIV algorithm and generated from three sources (1) pixel displacement, 2) seed density, 3) particle image size, and 4) flow gradients) are shown using PIV and hot wire data of a planar jet generated from a laminar channel flow. The effects of PIV uncertainty on turbulent

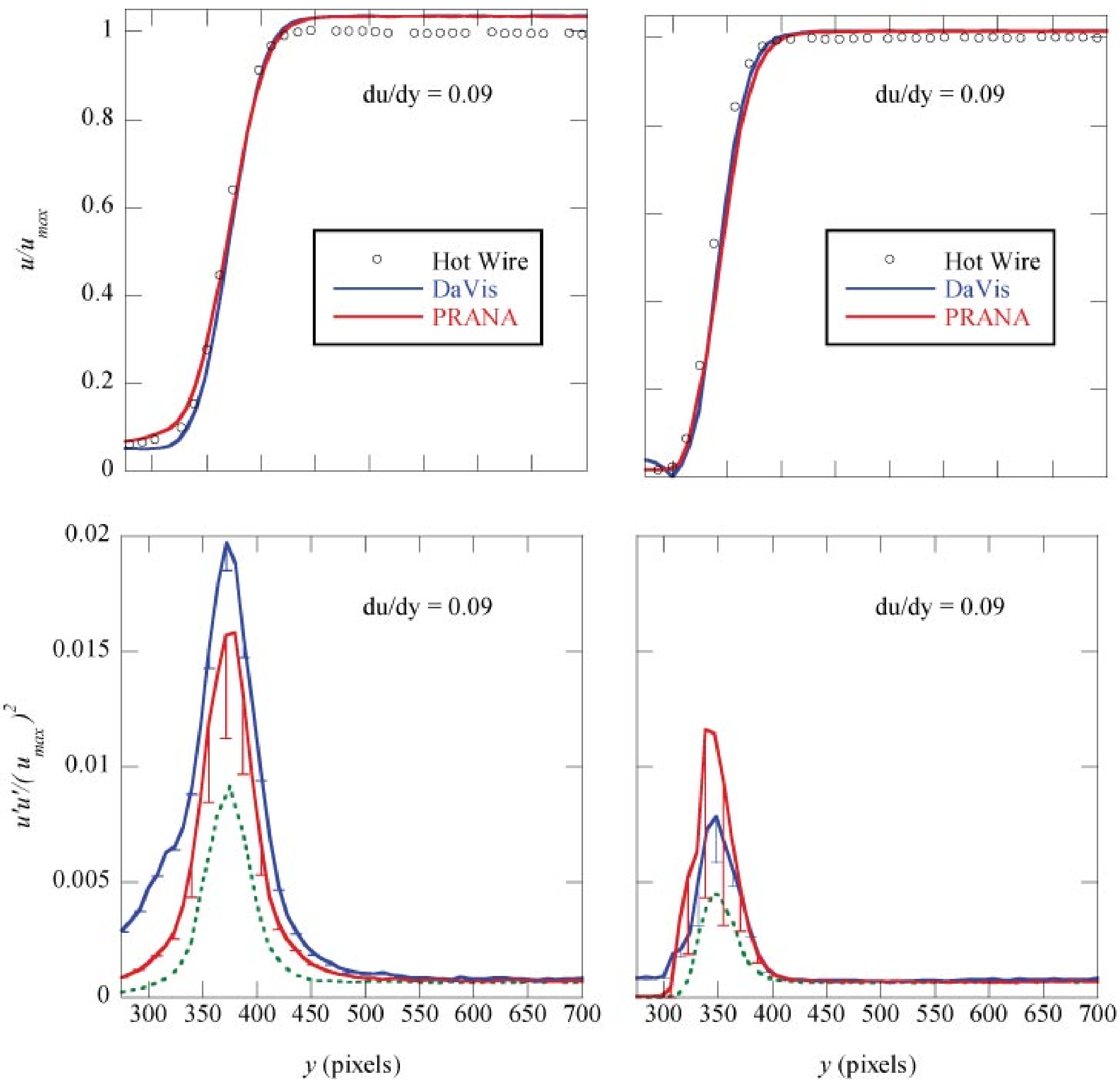


Figure 10: Cross stream profiles of the time-averaged velocity magnitude, $u$, and magnitude fluctuations, $\hat{u}\hat{u}$, for gradients of $du/dy \approx 0.09$ and 0.14 pixels/pixel from the hot wire, Davis, and PRANA measurements.

statistics, such as fluctuations, are also assessed. The results improve the application of PIV to M&S validation by better quantifying uncertainties on mean statistics and exposing increased errors on measured fluctuations.

The four sources studied generate errors affecting the rate at which converged statistics are acquired. These errors fluctuate on both sides of the mean and, when sufficient amounts of data are obtained, a converged mean that agrees with the hot wire solution is measured. However, this measurement noise increases the the measured velocity fluctuations reported by the PIV measurement system. These effects are observed for all four cases studied. Of the these, velocity gradients are the largest contributor to PIV error. Error estimation using results from Timmins *et al.* agree with the errors observed by the PIV algorithm.

For pixel displacements of $dx \leq \frac{1}{4}$ and $dx \geq \frac{5}{8}$ of the interrogation region size, the measured mean velocity was decreased. This is due to a combination of decreased dynamic range and sub-pixel interpolation uncertainties for the smaller pixel displacements and conditional averaging of larger velocities.

## References

[1] Nuclear Energy Agency, Committee of the Safety of Nuclear Installations, 2007, Best Practice Guidelines for the use of CFD in Nuclear Reactor Safety Applications. from www.oecd-nea.org/nsd/docs/2007.

[2] H. B. Lee and R. C. Bauer. Predictive computational fluid dynamics development and its verification and validation: an overview. In *ASME 2009 Fluids Engineering Division Summer Meeting*, 2009.

[3] B. H. Timmins, B. L. Smith, and P. P. Vlachos. Automatic particle image velocimetry uncertainty quantification. In *Proceedings of ASME Fluids Engineering Division Summer Meeting*, August 2010. Paper number FEDSM-ICNMM2010-30724.

[4] B. H. Timmins, B. L. Smith, and P. P. Vlachos. A method for automatic estimation of instantaneous local uncertainty in particle image velocimetry measurements. *submitted to Exp. Fluids*, 2011.

[5] M. Raffel, C. Willert, and J. Kompenhans. *Particle Image Velocimetry*. Springer-Verlag, Berlin Heidelberg, 1998.

[6] E. Lazar, B. DeBlauw, N. Glumac, C. Dutton, and G. Elliott. A practical approach to piv uncertainty analysis. In *27th AIAA Aerodynamic Measurement Technology and Ground Testing Conference*, number AIAA 2010-4355, Chicago, Illinois, 2010.

[7] Davis 7.2. LaVision GmbH, Göttingen, Germany.

[8] LaVision Inc. 301 W. Michigan Ave. Suite 403, Ypsilanti, MI 48197.

[9] A. C. Eckstein and P. P. Vlachos. Digital particle image velocimetry (DPIV) robust phase correlation. *Meas. Sci. and Tech.*, 20:055401, 2009.

[10] A. C. Eckstein and P. P. Vlachos. Assessment of advanced windowing techniques for digital particle image velocimetry (DPIV). *Meas. Sci. and Tech.*, 20:075402, 2009.

[11] J Nogueira, A Lecuona, S Nauri, M Legrand, and P A Rodrguez. Multiple t strategy for particle image velocimetry (piv) error correction, applied to a hot propulsive jet. *Measurement Science and Technology*, 20(7):074001, 2009.

[12] R. J. Adrian and J. Westerweel. *Particle Image Velocimetry*, volume I. Cambridge University Press, New York, 2011.

# Appendix A Magnitudes of Fluctuations

A single wire hot wire is sensitive to both the streamwise ($u_x$) and spanwise ($u_y$) velocity components, and therefore its output is essentially the magnitude of the velocity in the $x$ and $y$ directions. We assume that $u_z$ is very small in all of the cases presented here and that therefor $u^2 = {u_x}^2 + {u_y}^2$. This relationship is used to convert the PIV data into results comparable to the hot wire measurements. The hot wire probe must be equally sensitive to both components for this conversion to be accurate. The response of the single wire probe to velocity components normal to each other was assessed using a TSI hot wire calibrator that allows the probe to be rotated while maintaining the sensor position. This test yielded a difference in normal velocity components within 5%. We can write that, for the hot wire sensor,

$$\overline{(\overline{u} + u')^2} = \overline{(\overline{u}_x + u'_x)^2 + (\overline{u}_y + u'_y)^2}, \tag{8}$$

$$\overline{(\overline{u}^2 + 2\overline{u}u' + u'^2)} = \overline{\left[\overline{u}_x^2 + \overline{u}_y^2\right] + \left[u'^2_x + u'^2_y\right] + [2\overline{u}_x u'_x + 2\overline{u}_y u'_y]}. \tag{9}$$

An informative way to consider these equations is that the left hand side is what is measured by the hot wire while the right hand side can be obtained from the PIV measurement. The time-average of the cross terms is zero. This provides a root-mean-square relationship for the mean velocity and fluctuations components,

$$\overline{u^2} + \overline{u'^2} = \left[\overline{u_x^2} + \overline{u_y^2}\right] + \left[\overline{u'^2_x} + \overline{u'^2_y}\right]. \tag{10}$$

Using this relationship, a direct comparison of PIV and hot wire measurements can be made. For simplicity, all variables discussed throughout will be time-averaged values and the bars over the fluctuation variables will be dropped. This gives the magnitude statistics the relations,

$$\overline{u^2} = \left[\overline{u}_x^2 + \overline{u}_y^2\right], \tag{11}$$

$$u'u' = \left[u'^2_x + u'^2_y\right]. \tag{12}$$

Using this form, PIV data and hot wire data are directly comparable.